Citation for final published version:

Morini, L. , Tetik, Z. G., Shmuel, G. and Gei, M. 2020. On the universality of the frequency spectrum and band-gap optimisation of quasicrystalline-generated structured rods. Philosophical Transactions A: Mathematical, Physical and Engineering Sciences 378 (2162) , 20190240. 10.1098/rsta.2019.0240

Publishers page: http://dx.doi.org/10.1098/rsta.2019.0240

On the universality of the frequency spectrum and band-gap optimisation of quasicrystalline-generated structured rods

L. Morini[1], Z.G. Tetik[1], G. Shmuel[2], M. Gei[1]

[1]*School of Engineering, Cardiff University,*
15-17 The Parade, Cardiff CF24 3AA, Wales, UK.
[2]*Faculty of Mechanical Engineering,*
Technion-Israel Institute of Technology, Haifa, 32000, Israel.
E-mails: morinil@cardiff.ac.uk, geim@cardiff.ac.uk

August 21, 2019

Abstract

The dynamical properties of periodic two-component phononic rods whose elementary cells are generated adopting the Fibonacci substitution rules are studied through the recent-introduced method of the toroidal manifold. The method allows all band gaps and pass bands featuring the frequency spectrum to be represented in a compact form with a frequency-dependent flow line on the surface describing their ordered sequence. The flow lines on the torus can be closed or open: in the former case, (i) the frequency spectrum is periodic and the elementary cell corresponds to a canonical configuration, (ii) the band gap density depends on the lengths of the two phases; in the latter, the flow lines cover ergodically the torus and the band gap density is independent of those lengths. It is shown then how the proposed compact description of the spectrum can be exploited (i) to find the widest band gap for a given configuration and (ii) to optimise the layout of the elementary cell in order to maximise the low-frequency band gap. The scaling property of the frequency spectrum, that is a distinctive feature of quasicrystalline-generated phononic media, is also confirmed by inspecting band gap/pass band regions on the torus for elementary cells of different Fibonacci order.

Keywords: Fibonacci sequence, quasicrystalline phononic structure, metamaterial, band gap, Floquet-Bloch wave.

1 Introduction

In the last fifty years, the investigation of wave propagation in structured media and their applications in different areas of engineering has attracted significant interests from the scientific community. In this context, the contribution of Prof. Slepyan and his collaborators was essential for undestanding and predicting several phenomena, in particular transition waves in periodic and bistable structures (Nieves et al., 2017; Brun et al., 2013; Slepyan et al., 2005; Cherkaev et al., 2005), interaction between surface modes and fractures (Slepyan, 2010; Mishuris and Movchan, 2009), dissipation and phase transition in lattice materials (Slepyan, 2001c,b,a) and solitary nonlinear waves (Slepyan et al., 1998; Krylov et al., 1998). These fundamental studies, together with the results obtained by other authors (Ewing et al., 1956; Nemat-Nasser, 1972; Mead, 1998a,b), have inspired a very active field of research, concerning the design of phononic structures with the aim of achieving and controlling non-standard wave propagation phenomena, such as wave focussing (Guenneau et al., 2007), frequency filtering (Brun et al., 2010), cloaking (Norris, 2008; Colquitt et al., 2014) and negative refraction (Srivastava, 2016; Willis, 2016). Recently, the intriguing dynamical properties of a class of two-phase periodic structured solids whose unit cells are generated according to the Fibonacci substitution rule have been presented (Gei, 2010; Morini and Gei, 2018). This particular family of composites belongs to the subset of *quasicrystalline* media (Poddubny and Ivchenko, 2010) and portion of Floquet-Bloch frequency spectra of its members are characterised by a self-similar pattern which scales according to factors linked to the Kohmoto's invariant of the family itself (Kohmoto and Oono, 1984).

This work provides new insights on the relationship between the geometrical and constitutive properties of the elementary cells and the layout of pass bands/band gaps for the same type of quasicrystalline-generated phononic rods. By considering harmonic axial waves, we show that the corresponding frequency spectrum can be represented on a two-dimensional toroidal manifold similar to that introduced in Shmuel and Band (2016); Lustig and Shmuel (2018) to study Floquet-Bloch waves in periodic laminates. This manifold is universal for all two-phase configurations and the dispersion properties of the concerned rod can be inferred from the features of the frequency-parametrised flow lines lying on the toroidal domain, which is composed of band gap and pass band regions. We identify a particular subclass of rods whose flow lines on the torus are closed, thus describing a periodicity in the spectrum at increasing frequency, and show that the subclass coincides with that of the so-called *canonical structures* introduced by Morini and Gei Morini and Gei (2018). The local scaling governing the pass band/band gap layout about certain relevant frequencies (i.e. the *canonical frequencies*) is confirmed and highlighted through the analysis of the flow lines on the torus.

The universal representation of the spectrum on the toroidal surface allows us to rigorously estimate the band gap density for rods of any arbitrary Fibonacci elementary cell. We find that for canonical configurations this quantity varies with the ratio between the lengths of the phases, corresponding to the slope of the flow lines. Conversely, for generic non-canonical rods, the band gap density is independent of the lengths of the cells and is defined by the ratio between the area of the band gap subdomain and the total surface of the torus Barra and Gaspard (2000); Berkolaiko and Winn (2010); Band and Berkolaiko (2013). The provided examples show that this ratio can be easily evaluated numerically.

We further demonstrate how the compact representation of the spectrum on the two-dimensional torus can be exploited to either optimise the design of the elementary cells to achieve the widest low-frequency band gap or to determine rigorously where the maximal band gap is located in the spectrum for a given configuration. In the examples that we report we have based this investigation on analytical expressions of the boundaries of band gap regions that can be easily obtained for low-order elementary cells. Unlike the standard procedure based on partial evaluation of the spectrum Sigmund and Sondergaard Jensen (2003); Liu et al. (2014); Hedayatrasa et al. (2016), the proposed optimisation strategy provides exact rigorous results, and it can be easily generalised to Fibonacci cells of higher order.

2 Waves in quasicrystalline-generated phononic rods

We introduce a particular class of infinite, one-dimensional, two-component phononic rods consisting of a repeated elementary cell where two distinct elements, say L and S, are arranged in series according to the Fibonacci sequence (Poddubny and Ivchenko, 2010). The repetition of such a cell implies periodicity along the axis and then the possibility of applying the Floquet-Bloch technique in order to study harmonic wave propagation. The two-component Fibonacci sequence is based on the following substitution rule (Kolar and Ali, 1989):

$$L \to LS, \; S \to L. \tag{1}$$

Expression (1) implies that the i−th ($i = 0, 1, 2, \dots$) element of the Fibonacci sequence, here denoted by $\mathcal{F}_i$, obeys the recursive rule $\mathcal{F}_i = \mathcal{F}_{i-1}\mathcal{F}_{i-2}$, where the initial conditions are $\mathcal{F}_0 = S$ and $\mathcal{F}_1 = L$ (in Fig. 1, elementary cells designed according to sequences $\mathcal{F}_2$, $\mathcal{F}_3$ and $\mathcal{F}_4$ are displayed)[1]. The total number of elements of $\mathcal{F}_i$ corresponds to the Fibonacci number $\tilde{n}_i$ given by the recurrence relation $\tilde{n}_i = \tilde{n}_{i-1} + \tilde{n}_{i-2}$, with $i \geq 2$, and $\tilde{n}_0 = \tilde{n}_1 = 1$. The limit of $\tilde{n}_{i+1}/\tilde{n}_i$ for $i \to \infty$ corresponds to the so-called *golden* mean ratio $(1 + \sqrt{5})/2$.

Further in the text, we will refer to those structured rods as Fibonacci structures. According to the general criterion for the classification of the one-dimensional quasiperiodic patterns proposed in Kolar (1993), these structures are *quasicrystalline*. Quasicrystalline

---

[1] Henceforth, the notation $\mathcal{F}_i$ will indicate both the sequence and the elementary cell of the structured rod.

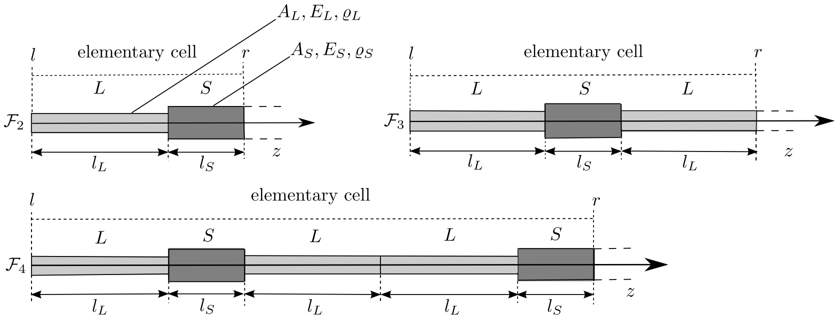

Figure 1: Elementary cells for infinite Fibonacci rods based on $\mathcal{F}_2 = LS$, $\mathcal{F}_3 = LSL$ and $\mathcal{F}_4 = LSLLS$. Symbols r and l denote right and left-hand boundaries of the cell, respectively.

media possess characteristic features that make them an intermediate class between periodic ordered crystals and random media (Steurer, 2004; Steurer and Deloudi, 2008). An example of these interesting and intriguing properties is the self-similarity of the frequency spectrum (Morini and Gei, 2018). The focus of this paper is on the analysis of the universal structure of this spectrum and on its application to predict, modulate and optimise the corresponding stop/pass band layout. We will show that the universality of the spectrum is closely related with the properties of the Floquet-Bloch dispersion relation exploited in Gei (2010) and summarised in this Section.

Let us introduce the mechanical and geometric parameters of elements L and S. The lengths of the two phases are indicated with l_L and l_S, respectively, while A_X, E_X and ϱ_X ($X \in \{L, S\}$) denote cross-section area of each bar, Young's modulus and mass density per unit volume of the two adopted materials, respectively. For both elements, we define the displacement function and the axial force along the rod as $u(z)$ and $N(z) = EAu'(z)$, respectively, where z is the coordinate describing the longitudinal axis. The governing equation of harmonic waves in each section assumes the form

$$u''_X(z) + \frac{\varrho_X}{E_X}\,\omega^2 u_X(z) = 0, \tag{2}$$

where $\omega \in \mathbb{R}^+$ is the circular frequency (simply the 'frequency' in the following) and the term ϱ_X/E_X corresponds to the reciprocal of the square of the speed of propagation of longitudinal waves in material X. The solution of (2) is given by

$$u_X(z) = C_1^X \sin\left(\sqrt{\frac{\varrho_X}{E_X}}\,\omega z\right) + C_2^X \cos\left(\sqrt{\frac{\varrho_X}{E_X}}\,\omega z\right), \tag{3}$$

where C_1^X and C_2^X are integration constants, to be determined by the boundary conditions.

To obtain the dispersion diagram of the periodic rod, displacement u_r and axial force N_r at the right-hand boundary of the elementary cell have to be given in terms of those at the left-hand boundary, namely u_l and N_l (Fig. 1), as

$$\boldsymbol{U}_r = \boldsymbol{T}_i \boldsymbol{U}_l, \tag{4}$$

where $\boldsymbol{U}_j = [u_j \;\; N_j]^T$ $(j = r, l)$ and $\boldsymbol{T}_i$ is a transfer (or transmission) matrix of the cell $\mathcal{F}_i$. This matrix is the result of the product $\boldsymbol{T}_i = \prod_{p=1}^{\tilde{n}_i} \boldsymbol{T}^X$, where $\boldsymbol{T}^X$ $(X \in \{L, S\})$ is the transfer matrix which relates quantities across a single element, given by

$$\boldsymbol{T}^X = \begin{bmatrix} \cos\left(\sqrt{\frac{\varrho_X}{E_X}}\,\omega l_X\right) & \frac{\sin\left(\sqrt{\frac{\varrho_X}{E_X}}\,\omega l_X\right)}{E_X A_X \sqrt{\frac{\varrho_X}{E_X}}\,\omega} \\ -E_X A_X \sqrt{\frac{\varrho_X}{E_X}}\,\omega \sin\left(\sqrt{\frac{\varrho_X}{E_X}}\,\omega l_X\right) & \cos\left(\sqrt{\frac{\varrho_X}{E_X}}\,\omega l_X\right) \end{bmatrix}. \tag{5}$$

Transfer matrices $\boldsymbol{T}_i$ have some important properties that can be exploited: i) they are unimodular, i.e. det $\boldsymbol{T}_i = 1$, and ii) follow the recursion rule

$$\boldsymbol{T}_{i+1} = \boldsymbol{T}_{i-1}\boldsymbol{T}_i, \tag{6}$$

with $\boldsymbol{T}_0 = \boldsymbol{T}^S$ and $\boldsymbol{T}_1 = \boldsymbol{T}^L$.

The Floquet-Bloch theorem implies that $\boldsymbol{U}_r = \exp(\mathrm{i}kL_i)\boldsymbol{U}_l$, where L_i is the total length of the fundamental cell $\mathcal{F}_i$ and the imaginary unit appearing in the argument of the exponential function should not be confused with the index i. By combining this condition with (4), we obtain the dispersion equation

$$\det[\boldsymbol{T}_i - e^{\mathrm{i}kL_i}\boldsymbol{I}] = 0. \tag{7}$$

The solution of eq. (7) provides the complete Floquet-Bloch spectrum and allows to obtain the location of band gaps and pass bands associated with the infinite rods here considered.

Equivalently, we can study the dispersion properties of these structures by evaluating the eigenvalues of the transfer matrix. As $\boldsymbol{T}_i$ is unimodular, it turns out that the characteristic equation of the waveguide is given by

$$\det[\boldsymbol{T}_i - \lambda\boldsymbol{I}] = 0 \quad \Rightarrow \quad \lambda^2 - \lambda\,\mathsf{tr}\,\boldsymbol{T}_i + 1 = 0. \tag{8}$$

By substituting $e^{\mathrm{i}kL_i} = \lambda$ in eq. (8) and multiplying it by $e^{-\mathrm{i}kL_i}$, the condition $e^{\mathrm{i}kL_i} + e^{-\mathrm{i}kL_i} - \mathsf{tr}\,\boldsymbol{T}_i = 0$ is achieved, leading to

$$\eta_i = \cos kL_i, \tag{9}$$

where $\eta_i = \mathsf{tr}\,\boldsymbol{T}_i/2$.

By observing eq. (9), we can easily deduce that all the information concerning harmonic axial wave propagation in a Fibonacci structure is contained in the half trace η_i of the corresponding transfer matrix. Waves propagate when $|\eta_i| < 1$ $(kL_i \in \mathbb{R}\backslash\{x : x = h\pi,\ h \in \mathbb{Z}\})$, band gaps correspond to the ranges of frequencies where $|\eta_i| > 1$ (k is a complex number with a non-vanishing imaginary part) whereas $|\eta_i| = 1$ characterises standing waves $(kL_i \in \{x : x = h\pi,\ h \in \mathbb{Z}\})$.

We note that both the transfer matrix (5) and the dispersion relation (9) possess a form identical to that derived in Lekner (1994); Rytov (1956) and used in Shmuel and Band (2016); Lustig and Shmuel (2018); Morini et al. (2019) to study antiplane shear waves in periodic two-phase, multi-phase and quasicrystalline laminates, respectively. Further in the paper, we will exploit this mathematical analogy generalising the approach proposed in Shmuel and Band (2016) to study the universal structure of the frequency spectrum of Fibonacci phononic rods.

3 Universal structure of the frequency spectrum

The analysis of the universal structure of the frequency spectrum will take advantage of the introduction of the following variables (Shmuel and Band, 2016; Barra and Gaspard, 2000; Berkolaiko and Winn, 2010; Band and Berkolaiko, 2013)

$$\zeta_X = \sqrt{\frac{\varrho_X}{E_X}}\omega l_X \quad (X \in \{L, S\}). \tag{10}$$

The unimodularity property of $\boldsymbol{T}_i$, together with the relationship (6), implies the following recursive rule for the half trace η_{i+1} (Morini and Gei, 2018):

$$\eta_{i+1} = 2\eta_i\eta_{i-1} - \eta_{i-2}, \quad \text{with} \quad i \geq 2, \tag{11}$$

where the initial conditions are

$$\eta_0(\zeta_S) = \cos\zeta_S, \quad \eta_1(\zeta_L) = \cos\zeta_L, \quad \eta_2(\zeta_S, \zeta_L; \gamma) = \cos\zeta_S\cos\zeta_L - \gamma\sin\zeta_S\sin\zeta_L. \tag{12}$$

The quantity

$$\gamma = \frac{1}{2}\left(\frac{A_L E_L}{A_S E_S}\sqrt{\frac{\varrho_L E_S}{\varrho_S E_L}} + \frac{A_S E_S}{A_L E_L}\sqrt{\frac{\varrho_S E_L}{\varrho_L E_S}}\right) \tag{13}$$

quantifies the impedance mismatch between the phases L and S, and it depends on their constitutive parameters but not on lengths of the single elements L and S. When $\gamma = 1$ there is no contrast between phases and the waveguide behaves as a homogeneous one. Expressions (12) show that for any given value of γ, η_0, η_1 and η_2 are $2\pi-$periodic functions of ζ_S and ζ_L. The generic half trace η_i can be derived by means of successive iterations of the recursive formula (11) by assuming (12) as initial conditions. Therefore, at any order i, η_i is also a $2\pi-$periodic function, separately, of ζ_S and ζ_L as it is defined through sums and products of functions with the same period. This implies that we can consider the half trace η_i as a function of a two-dimensional torus of edge length 2π, whose toroidal and poloidal coordinates are ζ_S and ζ_L, respectively. *This function is independent of the lengths of the two phases L and S.* The toroidal domain is composed of two complementary subspaces that are associated with the two inequalities introduced earlier in the discussion after eq. (9), namely: $|\eta_i(\zeta_S, \zeta_L)| < 1$ identifies a pass-band subdomain whereas $|\eta_i(\zeta_S, \zeta_L)| > 1$ corresponds to a band-gap one. The two regions might not be simply connected and the collection of lines of separation between the two subdomains, in which $|\eta_i(\zeta_S, \zeta_L)| = 1$, denotes a standing wave solution. The measures of the two regions are univocally determined by the value of the parameter γ.

A sketch of the toroidal domains for cells $\mathcal{F}_2$ and $\mathcal{F}_3$ are displayed in Fig. 2/(a) and /(b) where the set of physical properties tabled in Tab. 1 have been assumed (for that choice, $\gamma \approx 2.125$). In both plots, the pink zone corresponds to the pass-band region whereas the band-gap one is painted in gray.

Equation (9) shows that $|\eta_i(\zeta_S, \zeta_L)|$ is invariant under the transformation

$$\zeta_S \to \zeta_S + n\pi, \qquad \zeta_L \to \zeta_L + m\pi \qquad (n, m \in \mathbb{N}), \tag{14}$$

so that, as pointed out in Shmuel and Band (2016), the map on the torus can be equivalently represented on a reduced $\pi-$periodic torus. The latter can be conveniently represented through the so-called *square identification* (Arnold, 1989), in which the curved domain is flattened and transformed to a square whose edges are still described by coordinates ζ_S and ζ_L, both ranging now between 0 and π. In the new square representation, the band-gap subdomain ($|\eta_i(\zeta_S, \zeta_L)| > 1$) is denoted by $\mathbb{D}_i(\gamma)$. In the following, the square equivalent $\pi-$periodic torus with the domain $\mathbb{D}_i(\gamma)$ will be indicated with $\mathbb{T}_i$. At times, we will also refer to it as the 'reduced torus' for the cell $\mathcal{F}_i$.

In Fig. 2/(c) and /(d), the reduced tori $\mathbb{T}_2$ and $\mathbb{T}_3$ are reported. The light blue, light red and light brown regions in both plots denote the subdomains $\mathbb{D}_2(\gamma)$ and $\mathbb{D}_3(\gamma)$ determined for $\gamma \approx 8.031$, 2.125 and 1.170, respectively. In particular, the light red ones are the representation of the band gap domains depicted in gray on the original $2\pi-$periodic tori reported just above in the same Figure 2/(a) and /(b), respectively.

The spectrum for a Fibonacci rod of any arbitrary order can therefore be studied by analysing the dynamic flow parametrised $\boldsymbol{\zeta}(\omega) = (\zeta_S(\omega), \zeta_L(\omega))$ on the corresponding reduced torus, where the frequency ω plays the role of a time-like parameter. This flow is the image on $\mathbb{T}_i$ of the trajectories described by the angles ζ_S and ζ_L on the original torus. Two examples of the latter are the blue lines reported in Fig. 2 /(a) and /(b). In order to represent these flow lines on $\mathbb{T}_i$, we interpret expression (10) as the equation of a rectilinear trajectory lying on the square. Now, for any arbitrary Fibonacci cell $\mathcal{F}_i$ for which a specific indication for lengths l_L and l_S is provided, we can depict the trajectory (10) on $\mathbb{T}_i$ as those illustrated for $\mathcal{F}_2$ and $\mathcal{F}_3$ in the two plots of Fig. 2/(c) and /(d). For this purpose, if we consider values of the frequency such that $\sqrt{\varrho_X/E_X}\omega l_X > \pi$, by recalling the invariance of $\mathbb{T}_i$ and of its subdomain $\mathbb{D}_i(\gamma)$ with respect to transformations

$E_S = E_L = 3.3$ GPa	$\varrho_S = \varrho_L = 1140$ kg/m^3	$A_L = 4A_S = 1.963 \cdot 10^{-3}$ m^2	$l_L = 0.07$ m

Table 1: Mechanical and geometrical parameters adopted in the numerical calculations.

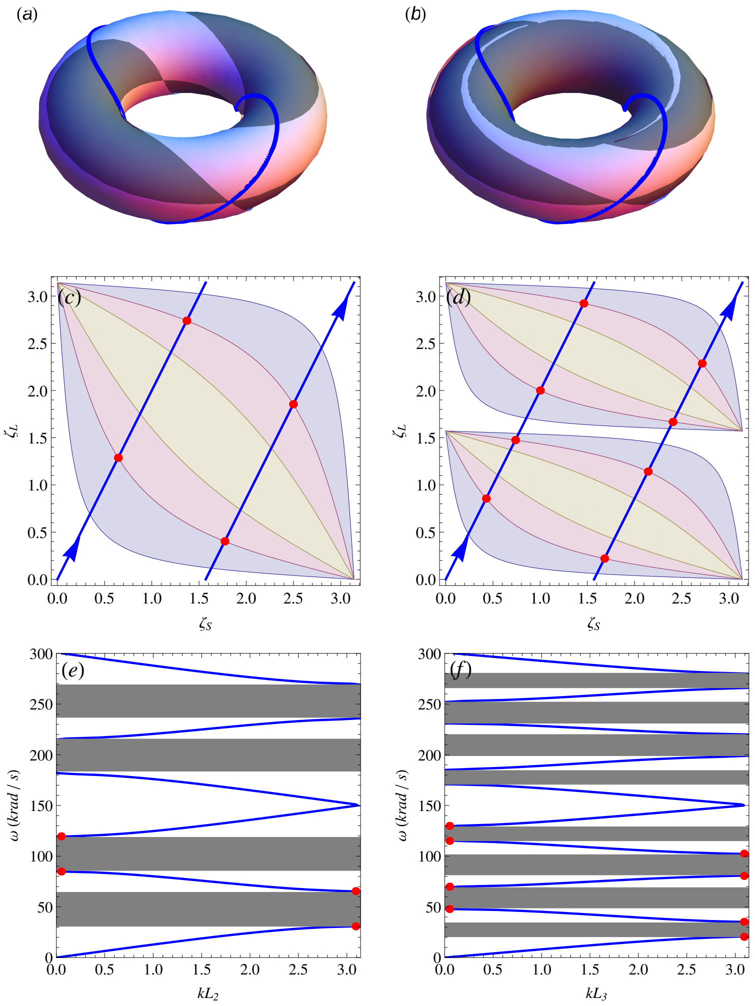

Figure 2: (a) and (b) Toroidal domains of edge length 2π for Fibonacci cells $\mathcal{F}_2$ (a) and $\mathcal{F}_3$ (b) with $\gamma \approx 2.125$. The pass-band regions where $|\eta_2| < 1$ and $|\eta_3| < 1$ are depicted in pink. The band-gap ones ($|\eta_2| > 1$ and $|\eta_3| > 1$) are highlighted in gray. An example of a periodic, closed flow line is reported in blue in each panel. (c) and (d) Square identification of the $\pi-$periodic torus for cells $\mathcal{F}_2$ and $\mathcal{F}_3$; light blue, light red and light brown regions correspond to the subdomains $\mathbb{D}_2(\gamma)$ and $\mathbb{D}_3(\gamma)$ defined for $\gamma \approx 8.031$ $(A_S/A_L = 0.0625)$, 2.125 $(A_S/A_L = 0.25)$ and 1.170 $(A_S/A_L = 0.5625)$, respectively. Red dots denote the intersection of the flow lines with the boundary of $\mathbb{D}_i$ for the case $\gamma \approx 2.125$. (e) and (f) Dispersion diagrams for Fibonacci cells $\mathcal{F}_2$ (e) and $\mathcal{F}_3$ (f) with $\gamma \approx$ 2.125 $(A_S/A_L = 0.25)$ and values of other the mechanical and geometrical parameters reported in Table 1.

(14), expression (10) can be written in the transformed form as

$$\zeta_S(\omega) = \sqrt{\frac{\varrho_S}{E_S}}\omega l_S - n\pi, \qquad \zeta_L(\omega) = \sqrt{\frac{\varrho_L}{E_L}}\omega l_L - m\pi \qquad (n, m \in \mathbb{N}). \tag{15}$$

Consequently, the trajectory (10) reported on $\mathbb{T}_i$ appears as a set of parallel segments as those reported in blue in Fig. 2/(c) and /(d), and the flow $\boldsymbol{\zeta}(\omega)$ can be expressed as

$$\boldsymbol{\zeta}(\omega) = \omega \left(\sqrt{\frac{\varrho_S}{E_S}} l_S, \sqrt{\frac{\varrho_L}{E_L}} l_L \right) \bmod \pi. \tag{16}$$

The segments shown in Fig. 2c) and d) are the images of the flow lines illustrated in Fig. 2/(a) and /(b), respectively. By examining these lines, we can easily observe that they trace a closed trajectory on the torus. In the next Section, the class of structures whose spectra are described by this particular type of flow lines is defined and characterised in details.

The values of ω for which the lines of the flow (16) intersect the boundary of the subdomain $\mathbb{D}_i(\gamma)$ coincide with the extremes of the band gaps. These intersections are highlighted with red points in Fig. 2/(c) and /(d) for waveguides generated by $\mathcal{F}_2$ and $\mathcal{F}_3$ for $\gamma \approx 2.125$. The same band gaps are illustrated in the classical dispersion diagrams of Fig. 2/(e) and /(f).

A parametric equation for the flow lines on $\mathbb{T}_i$ is easily derived from eqs. (15)

$$\zeta_L(\omega) = \alpha + \beta \zeta_S(\omega), \tag{17}$$

where

$$\alpha = \pi(\beta n - m) \tag{18}$$

and the angular coefficient

$$\beta = \sqrt{\frac{\varrho_L E_S}{\varrho_S E_L}} \frac{l_L}{l_S} \tag{19}$$

defines the direction of the flow (i.e. the slope of the blue segments shown in Fig. 2/(c) and /(d). In particular, the segment emerging from the origin for $\omega = 0^+$ (i.e. $m = n = 0$) has equation $\zeta_L(\omega) = \beta \zeta_S(\omega)$. In the next Section, we discuss how rational and irrational values of ratio (19) are associated with Fibonacci rods possessing periodic and non-periodic spectra, respectively, corresponding to closed and open trajectories on the $2\pi-$periodic torus, respectively. Both these two different behaviours are studied by analysing the flow lines on $\mathbb{T}_i$. Relevant indications concerning the band gap density and the different properties of rods with periodic and non-periodic spectra are obtained by using this universal approach.

4 Analysis of the flow lines on the reduced torus

Let us analyse the different types of trajectories (lines) that can describe the flow $\boldsymbol{\zeta}(\omega)$ on the torus. The condition for closed periodic lines is the existence of a frequency interval Ω such that (Arnold, 1989)

$$\zeta_S(\omega + \Omega) = \zeta_S(\omega) + 2\pi j, \qquad \zeta_L(\omega + \Omega) = \zeta_L(\omega) + 2\pi q \qquad (j, q \in \mathbb{N}). \tag{20}$$

By combining expressions (20) with eq. (10), we derive the relationships

$$\sqrt{\frac{\varrho_S}{E_S}}l_S = \frac{2\pi j}{\Omega}, \qquad \sqrt{\frac{\varrho_L}{E_L}}l_L = \frac{2\pi q}{\Omega}, \tag{21}$$

and then the ratio

$$\beta = \frac{q}{j}. \tag{22}$$

We can deduce from expression (22) that the trajectories on the torus are periodic if the ratio β is a rational number. This condition is exactly the same as that introduced in Morini and Gei (2018) and necessary to realise Fibonacci structures with a periodic spectrum, which are called in that article *canonical structures*. Therefore, canonical configurations correspond to closed flow trajectories on the torus. Considering the original 2π-periodic torus, these are closed helicoidal orbits on the surface as those reported in Figs. 2/(a) and /(b). The two whole numbers j and q represent the number of cycles, namely 2π rotations, about, respectively, the toroidal and poloidal axes. As an example, both blue trajectories of Figs. 2/(a) and /(b) correspond to $j = 1$ and $q = 2$ and then to $\beta = 2$. On $\mathbb{T}_i$, the closed flow lines associated with canonical structures become a *finite* number of parallel segments. The periodicity of the dispersion diagram is verified in Fig. 2/(e) and /(f) where the band gap limits already highlighted in the companion graphs plotted above (i.e. (c) and (d), respectively) are marked with red points.

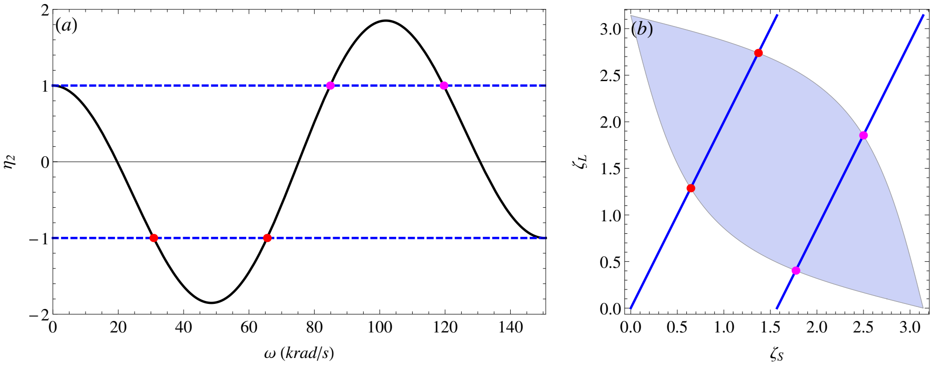

Figure 3: Half-trace function (a) and flow lines on diagram $\mathbb{T}_2$ (b) for a $\mathcal{F}_2$ canonical Fibonacci rod characterised by the parameters listed in Tab. 1 and $l_S/l_L = 1/2$ ($\gamma \approx 2.125$, $\beta = 2$). Coloured dots in both panels mark the extremes of the band gaps.

In Figs. 3, 4 and 5, examples of periodic flow lines for canonical structures generated by repetition of cells $\mathcal{F}_2$, $\mathcal{F}_3$ and $\mathcal{F}_4$ are reported. For the calculations, we considered two phases S and L of the same material ($E_S = E_L$ and $\varrho_S = \varrho_L$, see Tab. 1) so that parameters γ and β become

$$\gamma = \frac{1}{2}\left(\frac{A_S}{A_L} + \frac{A_L}{A_S}\right), \qquad \beta = \frac{l_L}{l_S}. \tag{23}$$

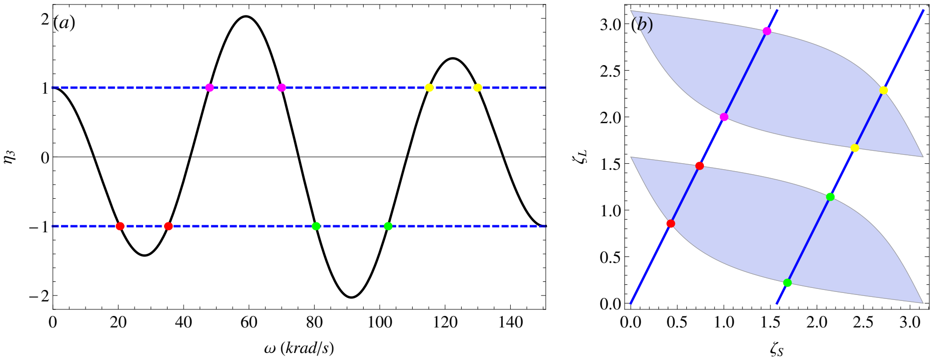

Figure 4: Half-trace function (a) and flow lines on diagram $\mathbb{T}_2$ (b) for a $\mathcal{F}_3$ canonical Fibonacci rod characterised by the parameters listed in Tab. 1 and $l_S/l_L = 1/2$ ($\gamma \approx 2.125$, $\beta = 2$). Coloured dots in both panels mark the extremes of the band gaps.

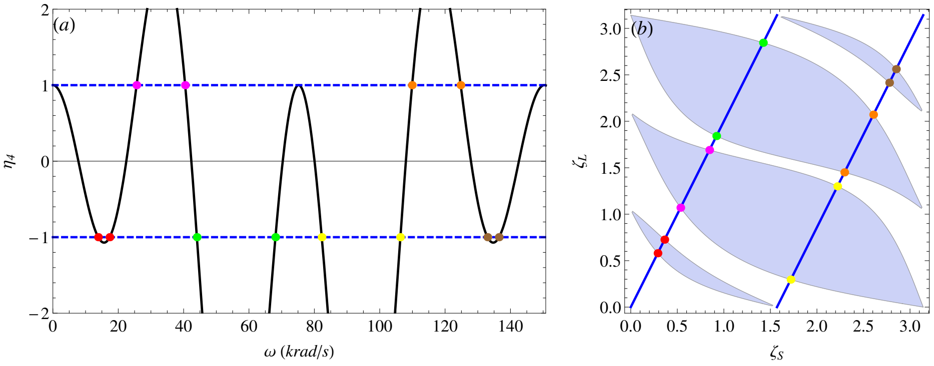

Figure 5: Half-trace function (a) and flow lines on diagram $\mathbb{T}_2$ (b) for a $\mathcal{F}_4$ canonical Fibonacci rod characterised by the parameters listed in Tab. 1 and $l_S/l_L = 1/2$ ($\gamma \approx 2.125$, $\beta = 2$). Coloured dots in both panels mark the extremes of the band gaps.

As a consequence, the areas of subdomains $\mathbb{D}_i$[2] depend only on ratio A_S/A_L, while the direction of flow is defined by l_S/l_L. Moreover, according to the classification provided in (Morini and Gei, 2018), the analysed rods belong to the second family of canonical configurations.

In the plots on the left-hand side of each of Figs. 3, 4 and 5, diagrams are presented of the half traces η_2, η_3, η_4 reported as functions of ω for an interval of frequencies which coincides with the half-period of the spectrum. We use coloured dots to earmark the extremes of the intervals where $|\eta_2|$, $|\eta_3|$, $|\eta_4| > 1$, defining the band gaps. The flow lines on $\mathbb{T}_2$, $\mathbb{T}_3$ and $\mathbb{T}_4$ are reported on the right-hand side of each figure. Their intersection with the boundaries of $\mathbb{D}_2$, $\mathbb{D}_3$ and $\mathbb{D}_4$, which identify the extreme of the band gaps, are indicated with the same coloured dots. We used the same colour cod in both diagrams of traces and $\mathbb{T}_i$ in order to associate the corresponding band gap in

---

[2] From now on the dependency on γ of $\mathbb{D}_i$ will be dropped.

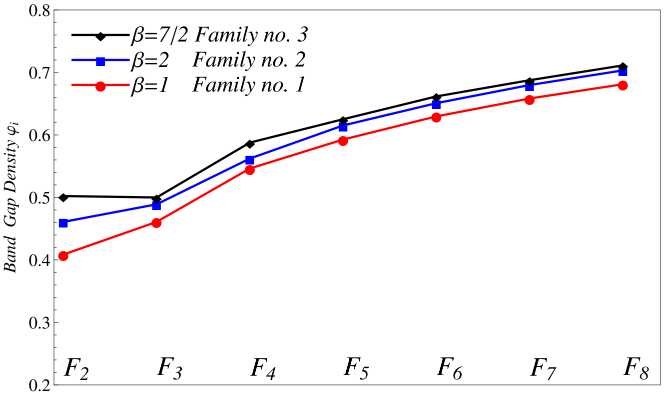

Figure 6: Band-gap density reported for Fibonacci canonical rods designed according to elementary cells $\mathcal{F}_2$ to $\mathcal{F}_8$ whose constitutive properties are listed in Tab. 1 ($\gamma \approx 2.125$). Three different values of the ratio l_S/l_L are assumed: 1, 1/2, 2/7, corresponding to $\beta = 1$ (Family no. 1), $\beta = 2$ (Family no. 2) and $\beta = 7/2$ (Family no. 3), respectively.

the two different representations. We note that the flow diagrams in $\mathbb{T}_i$ highlight all the band gaps contained in the half period of the canonical structures, and then the successive band gaps can be visualised using the same finite number of segments on $\mathbb{T}_i$ and applying the transformation (15). Therefore, for canonical structures generated by any arbitrary cell $\mathcal{F}_i$, the band gap density φ_i is given by the ratio between the measure of the intersections between the flow lines and the subdomain $\mathbb{D}_i$, and the total length of the flow lines. The latter is given by the sum of all the parallel segments reported in Figs. 3, 4 and 5 and corresponding to $\sqrt{j^2 + q^2}\pi$. This ratio depends on both the area of $\mathbb{D}_i$ and the direction of the flow lines, and then on both γ and β parameters.

The values of the band gap density for three different examples of canonical structures with elementary cells from $\mathcal{F}_2$ to $\mathcal{F}_8$ are reported in Fig. 6. We assumed the same constitutive properties used for the results shown in Figs. 3, 4 and 5 (see Tab. 1) and three different ratios l_S/l_L which, in this particular case, correspond to three values of β, namely 1, 2 and 7/2 (see eq. $(23)_2$). According to the definition provided in Morini and Gei (2018), those three ratios are associated with canonical structures which belong to the first, the second and the third family, respectively. The three families are distinguished by different stop and pass band layouts, but they all possess periodic spectra with properties depending exclusively on β. Fig. 6 shows that the value of the band gap density is different for cells of the same order i, but with distinct values of the parameter β. This confirms, as we have already mentioned, that the band gap density of canonical rods depends on the ratio l_S/l_L. As a consequence, if we assume given constitutive properties of the phases S and L (i.e. E_S, E_L, ϱ_S and ϱ_L) and given cross sections A_L and A_S, and then we determine univocally the domain $\mathbb{T}_i$ and the area of the subspace $\mathbb{D}_i$, we can modulate the band gap density by simply varying the ratio l_S/l_L. Indeed, by changing this parameter, we assign a different direction to the flow lines on the torus or equivalently to the slope of the segments on the square identification of $\mathbb{T}_i$, determining the band gap intervals which coincide with intersections of the flow trajectories with the subdomain $\mathbb{D}_i$.

By observing Fig. 6, we note that, for all the three types of canonical rods here analysed, the band gap density increases with the index i following a logarithmic trend. This is in agreement with the results presented in Kohmoto et al. (1987); Sutherland and Kohmoto (1987) for electronic and optic systems subjected to quasiperiodic Fibonacci potentials.

In addition to the canonical ones, we can define a different class of waveguides whose ratio β is irrational. In this case, the spectrum is not periodic and the corresponding flow lines are open and cover *ergodically* the whole torus with uniform measure (Katok and Hasselblatt, 1996). In this situation, it is commonly said that the orbits are *dense* on the torus (Ott, 1993). Consequently, the flow trajectories on $\mathbb{T}_i$ consist of an *infinite* number of parallel segments which in turn cover ergodically the whole square domain. Therefore, the band gap density is given by the ratio between the area of the subdomain $\mathbb{D}_i$ and the area π^2 of the square. Since the measure of $\mathbb{D}_i$ is determined only by the parameter γ, which is independent of the ratio l_S/l_L, for non-canonical rods the band gap density does not depend on that ratio.

The fundamental differences between the flow lines of a canonical waveguide and those of non-canonical one are pointed out in Fig. 7. Figs. 7/(a) and 7/(b) display the variation of the half trace η_2 with the frequency and the trajectories on the reduced torus $\mathbb{T}_2$ for a canonical structure with parameters listed in Tab. 1 and $l_S/l_L = 1/2$, the same considered in Fig. 3. The variation of η_2 is plotted for a frequency range equal to its period ($0 < \omega \lesssim 305$ krad/s). The corresponding extremes of band gaps both in the half trace diagram and in $\mathbb{T}_2$ are marked using points with the same colours. As anticipated, due to the periodicity of the flow lines, all band gaps and pass bands in the frequency spectrum can be represented through the two parallel segments reported in Fig. 7/(b). Indeed, by observing this figure, the first and the third band gap, whose extremes are denoted by red and green points, respectively, overlap as well as the second and the fourth ones whose extremes are marked with magenta and yellow points, respectively.

The pairs of figures 7/(c) and 7/(d), 7/(e) and 7/(f), and 7/(g) and 7/(h) illustrate the diagrams of the half trace η_2 and the flow lines on $\mathbb{T}_2$ for cells $\mathcal{F}_2$ with $l_S/l_L = 1/2 + \sqrt{1/500}$, $l_S/l_L = 1/2 + 3\sqrt{1/500}$ and $l_S/l_L = 1/2 + 10\sqrt{1/500}$, respectively. We assumed three different perturbations of the length ratio in order to have three irrational values of β and then three examples of non-canonical configurations. Their spectra are studied in the same range of frequencies of the canonical waveguide in Figs. 7/(a) and 7/(b). We observe that for the three irrational ratios the half trace η_2 is no longer periodic, and the number of band gaps in the same frequency range increases with respect to the canonical case. Due to the lack of periodicity, band gaps are characterised by widths and relative distances that are all different from each other. This implies that

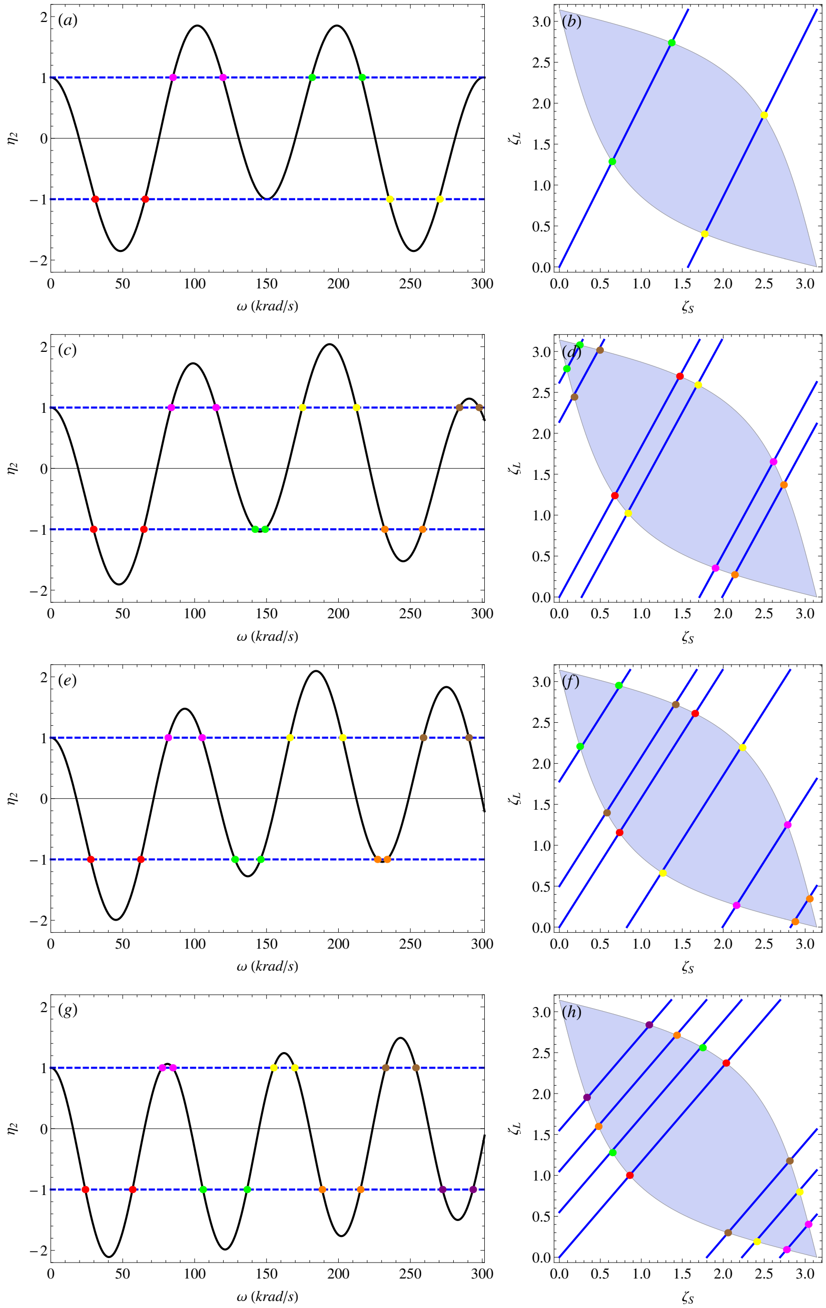

Figure 7: Half-trace diagrams and flow lines on $\mathbb{T}_2$ associated with cells $\mathcal{F}_2$ characterised by the parameters listed in Tab. 1 and (a)–(b) $l_S/l_L = 1/2$, (c)–(d) $l_S/l_L = 1/2 + \sqrt{1/500}$, (e)–(f) $l_S/l_L = 1/2 + 3\sqrt{1/500}$, (g)–(h) $l_S/l_L = 1/2 + 10\sqrt{1/500}$. In Coloured dots mark the extremes of homologous band gaps.

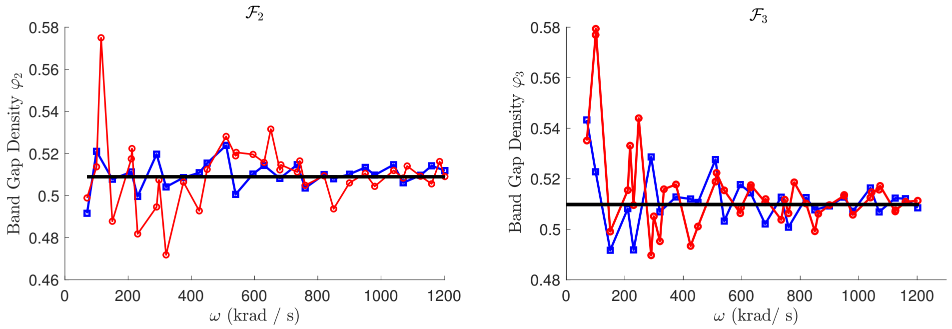

Figure 8: Numerical study of convergence of the band-gap density for non-canonical structures with elementary cells $\mathcal{F}_2$ and $\mathcal{F}_3$ whose properties are listed in Tab. 1 ($\gamma \approx 2.125$). We assumed two irrational values for the length ratio, i.e. $l_S/l_L = \sqrt{3/10}$ (red circle markers) and $l_S/l_L = \sqrt{1/2}$ (blue square markers).

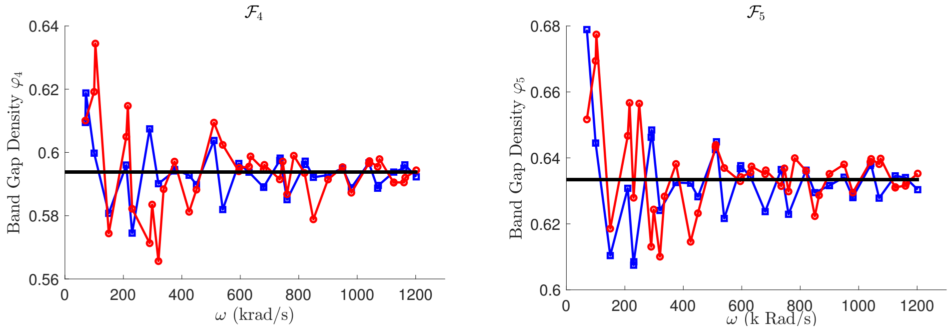

Figure 9: Numerical study of convergence of band-gap density for non-canonical structures with elementary cells $\mathcal{F}_4$ and $\mathcal{F}_5$ whose properties are listed in Tab. 1 ($\gamma \approx 2.125$). We assumed two irrational values for the length ratio, i.e. $l_S/l_L = \sqrt{3/10}$ (red circle markers) and $l_S/l_L = \sqrt{1/2}$ (blue square markers).

the representation of each of them on $\mathbb{T}_2$ is associated with a different parallel segment, as shown in Figs. $7/(d)$, $7/(f)$ and $7/(h)$. These segments are the image on the reduced torus of the three flow lines, which in this case are infinite. At an increase of the frequency range for the half traces in Figs. $7/(c)$, $7/(e)$ and $7/(g)$, more and more segments are needed in order to depict the set of band gaps on the right-hand counterparts (Figs. $7/(d)$, $7/(f)$ and $7/(h)$, respectively), up to cover the whole domain of $\mathbb{T}_2$. Therefore, for all the three non canonical rods analysed, it is confirmed that the band gap density φ_i is given by the ratio between the area of $\mathbb{D}_2$ and π^2. In general,

$$\varphi_i = \frac{1}{\pi^2} \int\int_{\mathbb{D}_i(\gamma)} d\zeta_S d\zeta_L. \tag{24}$$

Unlike canonical structures, this value is univocally determined by the parameter γ and is *independent* of l_S/l_L.

We can now generalise the analysis provided for waveguides generated by $\mathcal{F}_2$ to any arbitrary Fibonacci cell $\mathcal{F}_i$. In analogy with the previous examples, we consider two phases with the same properties (see Tab. 1) and $l_S/l_L = \sqrt{3/10}$ and $l_S/l_L = \sqrt{1/2}$, corresponding to $\beta = \sqrt{10/3}$ and $\beta = \sqrt{2}$, respectively. We solve numerically the dispersion relation (9) over increasing intervals of frequencies, and at each iteration we estimate the ratio between the total length of the band gaps and the whole length of the frequency range. Calculations are carried out for structures designed according to cells $\mathcal{F}_2$, $\mathcal{F}_3$, $\mathcal{F}_4$ and $\mathcal{F}_5$; the results are shown in Figs. 8 and 9. Red lines with circle marks and blue lines with square marks map the band gap density for $l_S/l_L = \sqrt{3/10}$ and $l_S/l_L = \sqrt{1/2}$, respectively. For both cases, and in each panel, we note the convergence of the data to the black horizontal line that corresponds to φ_i in (24). These ratios can be estimated numerically or analytically for cell $\mathcal{F}_2$ (see explicit expression derived in Shmuel and Band (2016)), and in this case they are 0.5090 for $\mathcal{F}_2$, 0.5098 for $\mathcal{F}_3$, 0.5938 for $\mathcal{F}_3$ and 0.6334 for $\mathcal{F}_5$. The convergence observed for all panels in Figs. 8 and 9 demonstrates that for non-canonical structures the band gap density at a given value of γ is *independent* of the lengths of the phases S and L. Therefore, we can state that the band gap density is a *universal* property of classes of non canonical waveguides characterised by a prescribed γ and an elementary cell $\mathcal{F}_i$. This is in agreement with the results reached in Shmuel and Band (2016), where it is shown that for irrational values of a parameter analogous to our β the band gap density of two phase laminates is independent of the thicknesses of the layers.

5 Band gap optimisation using universality properties

The compact representation of the frequency spectrum on $\mathbb{T}_i$ is now used to formulate rigorously and solve two types of optimisation problems in periodic quasicrystalline-generated rods. We focus on the case of $\mathcal{F}_3$ for which analytical representations of the boundaries of the band gaps are available, but the same approach can be easily applied to higher-order cells with the aid of implicit expressions similar to those obtained in Lustig and Shmuel (2018).

The band gap subdomain $\mathbb{D}_3$ is composed of two identical regions for any values of the parameter γ: one, namely $\mathbb{D}_3^-$, lies on the portion of $\mathbb{T}_3$ delimited by the intervals $0 \leq \zeta_S \leq \pi$ and $0 \leq \zeta_L \leq \pi/2$; the other, $\mathbb{D}_3^+$, occupies the portion delimited by the intervals $0 \leq \zeta_S \leq \pi$ and $\pi/2 \leq \zeta_L \leq \pi$ (see Figs. 2/(d) and 4/(b)). The former is considered for the maximisation of gap width, but the same methodology can be applied to $\mathbb{D}_3^+$. All points of the boundary of $\mathbb{D}_3^-$ satisfy the condition $\eta_3(\zeta_S, \zeta_L) = -1$ and define the curves $\mathcal{C}_l^-$ and $\mathcal{C}_u^-$ whose analytical expressions are

$$\zeta_L = \arctan\left[\frac{(\gamma \pm \sqrt{\gamma^2 - 1})\sin\zeta_S}{1 - \cos\zeta_S}\right], \tag{25}$$

where the upper curve $\mathcal{C}_u^-$ (lower one $\mathcal{C}_l^-$) corresponds to the plus (minus) sign in the numerator. The width of the generic band gap $\{\omega^B - \omega^A\}$ is related to the length of the associated interval along the flow line, whose endpoints $A(\zeta_S^A, \zeta_L^A)$ and $B(\zeta_S^B, \zeta_L^B)$ lie on $\mathcal{C}_u^-$ and $\mathcal{C}_l^-$, respectively, through the relationship

$$\omega^B - \omega^A = \frac{\nu_S}{\sqrt{1+\beta^2}} \sqrt{(\zeta_S^B - \zeta_S^A)^2 + (\zeta_L^B - \zeta_L^A)^2}, \tag{26}$$

where $\nu_S = \sqrt{E_S}/(\sqrt{\varrho_S} l_S)$. An equation analogous to (26) is obtained in Shmuel and Band (2016), where it is used to derive exact expressions for the bounds of the band-gap widths in two-phase laminates as functions of the geometrical and physical properties of the unit cells. Since points A and B belong to the flow lines on $\mathbb{T}_3$, their coordinates satisfy the relationships

$$\zeta_L^A = \beta\zeta_S^A + \alpha, \qquad \zeta_L^B = \beta\zeta_S^B + \alpha, \tag{27}$$

where $\zeta_X^\bullet = \zeta_X(\omega^\bullet)$. Equations (26) and (27), together with expressions (25) for the curves $\mathcal{C}_l^-$ and $\mathcal{C}_u^-$, enable us to maximise the width of $\{\omega^B - \omega^A\}$ through the flow lines defined on the basis of the physical and geometrical properties of the elementary cells.

5.1 Identification of the widest band gap for a prescribed structure

We first consider a given cell $\mathcal{F}_3$ with prescribed physical and geometrical properties. Our purpose is to determine the interval $\{\omega^B - \omega^A\}$ defining the widest band gap in the frequency spectrum of the structure. As $\beta = (\zeta_L^B - \zeta_L^A)/(\zeta_S^B - \zeta_S^A)$, expression (26) can be written in the form

$$\omega^B - \omega^A = \nu_S(\zeta_S^B - \zeta_S^A) = \nu_S \Delta\zeta_S. \tag{28}$$

In this case, ν_S and β are known and the goal is achieved by finding the value of the translation coefficient α associated with the largest $\Delta\zeta_S$. By imposing that both the points A and B lie on the flow line (27) and that $A \in \mathcal{C}_l^-$ and $B \in \mathcal{C}_u^-$, the following equations for the coordinates ζ_S^B and ζ_S^A are established

$$\beta\zeta_S^A + \alpha = \arctan\left[\frac{(\gamma - \sqrt{\gamma^2-1})\sin\zeta_S^A}{1-\cos\zeta_S^A}\right], \tag{29}$$

$$\beta\zeta_S^B + \alpha = \arctan\left[\frac{(\gamma + \sqrt{\gamma^2-1})\sin\zeta_S^B}{1-\cos\zeta_S^B}\right], \tag{30}$$

and then $\Delta\zeta_S = \zeta_S^B - \zeta_S^A$ becomes

$$\Delta\zeta_S = \frac{1}{\beta}\left\{\arctan\left[\frac{(\gamma + \sqrt{\gamma^2-1})\sin\zeta_S^B}{1-\cos\zeta_S^B}\right] - \arctan\left[\frac{(\gamma - \sqrt{\gamma^2-1})\sin\zeta_S^A}{1-\cos\zeta_S^A}\right]\right\}. \tag{31}$$

By eliminating α between (29) and (30), it turns out that

$$\Delta\alpha = \beta(\zeta_S^B - \zeta_S^A) - \arctan\left[\frac{(\gamma + \sqrt{\gamma^2 - 1})\sin\zeta_S^B}{1 - \cos\zeta_S^B}\right] + \arctan\left[\frac{(\gamma - \sqrt{\gamma^2 - 1})\sin\zeta_S^A}{1 - \cos\zeta_S^A}\right] = 0. \tag{32}$$

The aim is now to determine the values of ζ_S^A and ζ_S^B that maximise the quantity (31) and are solution of eq. (32). Then, the corresponding α can be evaluated by means of (29) and (30). The problem can be solved graphically for any cell $\mathcal{F}_3$ through the two diagrams reported in Fig. 10. For the calculations we considered a non-canonical configuration with the parameters listed in Tab. 1 and $l_S/l_L = 1/2 + 3\sqrt{1/500}$.

The contour plot in Fig. $10/(a)$ shows the variation of the function (31) on the whole two-dimensional domain $0 \leq \{\zeta_S^A, \zeta_S^B\} \leq \pi$, while the red line reported in the same figure is determined by the values of ζ_S^A and ζ_S^B satisfying eq. (32). Point P, whose coordinates are solution to (32) and maximise $\Delta\zeta_S$, is denoted by the yellow dot. It corresponds to the intersection between the red line and the blue curve, defined in this case through the equation $\Delta\zeta_S = 0.589$. We note that this point also coincides with the intersection between the curve (32) and the line $\zeta_S^B = \pi - \zeta_S^A$. Consequently, the coordinates ζ_S^A and ζ_S^B can be derived as the solution of the system

$$\begin{cases} \Delta\alpha(\zeta_S^A, \zeta_S^B) = 0, \\ \zeta_S^B + \zeta_S^A = \pi. \end{cases} \tag{33}$$

By substituting $(33)_2$ into $(33)_1$, we obtain

$$\begin{cases} \arctan\left[\frac{(\gamma - \sqrt{\gamma^2-1})\sin\zeta_S^A}{1-\cos\zeta_S^A}\right] - \arctan\left[\frac{(\gamma + \sqrt{\gamma^2-1})\sin(\pi-\zeta_S^A)}{1-\cos(\pi-\zeta_S^A)}\right] + \beta(\pi - 2\zeta_S^A) = 0, \\ \zeta_S^B = \pi - \zeta_S^A. \end{cases} \tag{34}$$

For the set of physical and geometrical properties assumed in the example, the solution of (34) is $\zeta_S^A = 1.278$ and $\zeta_S^B = 1.863$. Using these values in eq. (29) (or (30)), $\alpha = 1.692$ is determined. Remembering that in this case $l_S/l_L = 1/2 + 3\sqrt{1/500} = 1/\beta$, eqs. (27) provide $\zeta_L^A = 0.324$ and $\zeta_L^B = 1.246$.

We determined the translation coefficient of the flow segment corresponding to the widest band gap among all those detected in the spectrum of the structure, as well as the coordinates on $\mathbb{T}_3$ of the points $A(\zeta_S^A, \zeta_L^A)$ and $B(\zeta_S^B, \zeta_L^B)$, associated with ω^A and ω^B. A and B are denoted by red dots in Fig. $11/(b)$, and the width $\omega^B - \omega^A = 22.066$ krad/s can be calculated through eq. (28). On the basis of the definition (15), ω^A and ω^B are given by

$$\omega^A = \frac{1}{l_S}\sqrt{\frac{E_S}{\varrho_S}}(\zeta_S^A + n\pi), \qquad \omega^B = \frac{1}{l_S}\sqrt{\frac{E_S}{\varrho_S}}(\zeta_S^B + n\pi), \tag{35}$$

or, alternatively,

$$\omega^A = \frac{1}{l_L}\sqrt{\frac{E_L}{\varrho_L}}(\zeta_L^A + m\pi), \qquad \omega^B = \frac{1}{l_L}\sqrt{\frac{E_L}{\varrho_L}}(\zeta_L^B + m\pi), \tag{36}$$

where n and m are two whole numbers satisfying condition (18).

The invariance of $\mathbb{T}_3$ and $\mathbb{D}_3$ with respect to the transformations (14), together with the conditions $A \in \mathcal{C}_l^-$ and $B \in \mathcal{C}_l^+$, provides the following system of implicit equations

$$\begin{cases} \eta_3(\zeta_S^A + n\pi, \zeta_L^A + m\pi) = -1, \\ \eta_3(\zeta_S^B + n\pi, \zeta_L^B + m\pi) = -1. \end{cases} \tag{37}$$

The values of n and m corresponding to the extremes ω^A and ω^B of the maximal band gap are given by a pair of integer solutions of system (37) that satisfies the relationship (18). They can be found through a diagram like the one reported in Fig. 10/(b), where the solutions of eqs. $(37)_1$ and $(37)_2$ correspond to the red and blue contours, respectively, and the black line is defined by eq. (18). The green dot denotes the intersection of the three curves at $n = 6$ and $m = 10$, which are the required numbers in this case. By substituting them together with the previously calculated ζ_S^A, ζ_S^B, ζ_L^A, ζ_L^B and the physical properties of the cell in expressions (35) and (36), we finally determine $\omega^A = 759.69$ krad/s and $\omega^B = 781.76$ krad/s. These extremal values are highlighted using the red dots in the diagram of the half trace η_3 reported in Fig. 11/(a).

The illustrated method can be easily applied to cells of higher order through the general approach developed in Lustig and Shmuel (2018), where analytical expressions for the boundaries of the band gap subregions of periodic laminates with an arbitrary number of phases are derived. This original procedure provides several fundamental advantages with respect to the standard optimisation methods based on the numerical evaluation of the frequency spectrum. This is obvious especially in the case of non-canonical structures as this is the case where the spectrum is not periodic, and then, in principle, calculations over an infinite frequency domain should be performed to determine the widest band gap. Since in practice calculations must be truncated, such an approach yields only an approximate solution. Moreover, there is currently any rigorous way to predict how the considered truncated subdomain allows an accurate estimation compared to the real infinite case. Contrarily, through the formulation over the torus $\mathbb{T}_3$, the problem is solved in closed form, without any approximation, avoiding the numerical calculations required by the evaluation of large portions of the frequency spectrum. It is also worth remarking that the solutions m and n can be relatively high, at a frequency for which, due to the effects of lateral inertia, the simple one-dimensional axial model might be no longer valid.

5.2 Optimisation of the lowest band gap through variation of the geometrical properties

The second example of optimisation which can be formulated rigorously and solved by exploiting the representation of the spectrum on $\mathbb{T}_3$ is here illustrated. Let us consider a cell $\mathcal{F}_3$ with parameters listed in Tab. 1, such that $\gamma \approx 2.125$ and the slope of the flow lines becomes $\beta = l_L/l_S$. Our aim is now to find the value of β that maximise the lowest band gap of the spectrum.

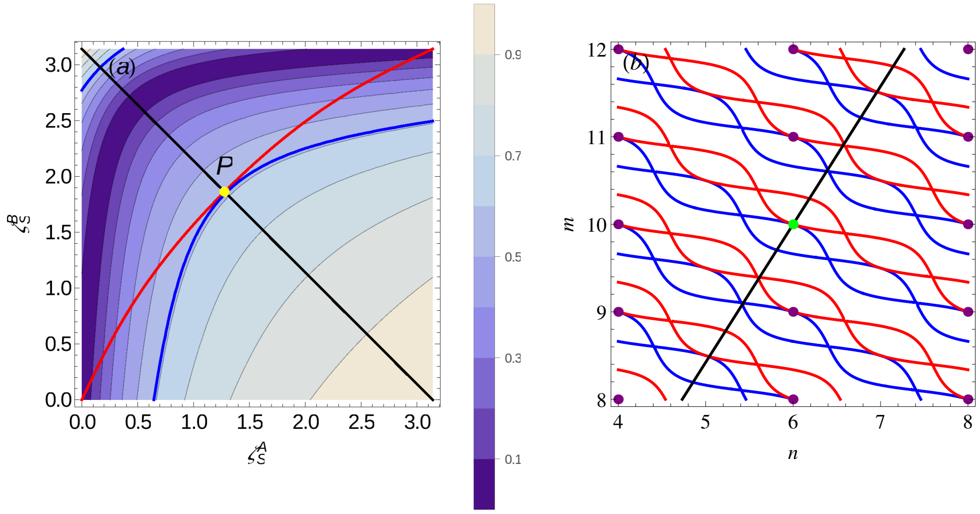

Figure 10: Widest band gap for a non-canonical cell $\mathcal{F}_3$ designed assuming the parameters listed in Tab. 1 and $l_S/l_L = 1/2 + 3\sqrt{1/500}$. (a) Contour plot of the function $\Delta\zeta_S(\zeta_S^A, \zeta_S^B)$. Red, blue and black lines are associated with eqs. $\Delta\alpha(\zeta_S^A, \zeta_S^B) = 0$, $\Delta\zeta_S(\zeta_S^A, \zeta_S^B) = 0.589$ and $\zeta_S^B + \zeta_S^A = \pi$, respectively. (b) Graphic solution of system including eqs. (18) and (37); red, blue and black lines correspond to eqs. $(37)_1$, $(37)_2$ and (18), respectively; the green dot is placed at $n = 6$, $m = 10$.

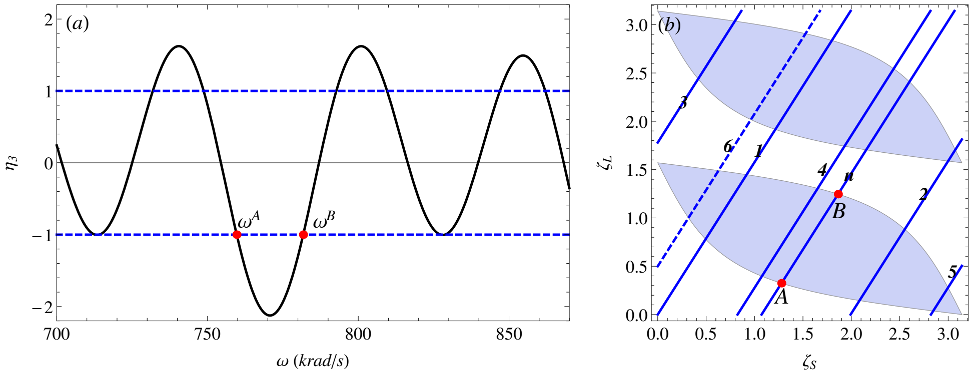

Figure 11: Widest band gap for a non-canonical cell $\mathcal{F}_3$ designed assuming the parameters listed in Tab. 1 and $l_S/l_L = 1/2 + 3\sqrt{1/500}$, highlighted both on the diagram of the half trace η_3 (a) and on the reduced torus $\mathbb{T}_3$ (b). The extremes of the gap, namely $\omega^A = 759.69$ krad/s and $\omega^B = 781.76$ krad/s (a) and $A(\zeta_S^A, \zeta_L^A)$ and $B(\zeta_S^B, \zeta_L^B)$ on $\mathbb{T}_3$ (b), are marked with red points.

This one, i.e. $\{\omega^B - \omega^A\}$, is detected by the intersection between the region $\mathbb{D}_3^-$ and the flow segment starting from the origin of the plane $O\zeta_S\zeta_L$. Similarly to the case studied in Section 5.1, $A(\zeta_S^A, \zeta_L^A) \in \mathcal{C}_l^-$ and $B(\zeta_S^B, \zeta_L^B) \in \mathcal{C}_l^+$, and

$$\zeta_L^A = \beta\zeta_S^A, \qquad \zeta_L^B = \beta\zeta_S^B, \tag{38}$$

since $\alpha = 0$ in this problem. Equation $(38)_1$, together with the condition $A \in \mathcal{C}_l^-$, provides the following expression for β:

$$\beta = \frac{1}{\zeta_S^A} \arctan \left[\frac{(\gamma - \sqrt{\gamma^2 - 1}) \sin \zeta_S^A}{1 - \cos \zeta_S^A} \right]. \tag{39}$$

By substituting (39) into $(38)_2$ and imposing $B \in \mathcal{C}_u^-$, we get

$$\arctan \left[\frac{(\gamma + \sqrt{\gamma^2 - 1}) \sin \zeta_S^B}{1 - \cos \zeta_S^B} \right] + \frac{\zeta_S^B}{\zeta_S^A} \arctan \left[\frac{(\gamma - \sqrt{\gamma^2 - 1}) \sin \zeta_S^A}{1 - \cos \zeta_S^A} \right] = 0. \tag{40}$$

Assuming that l_S, and then ν_S, is known, the expression for the width of the band gap (26) can be written in the normalised form

$$\Delta\overline{\omega} = \frac{\omega^B - \omega^A}{\nu_S} = \frac{\sqrt{(\zeta_S^B - \zeta_S^A)^2 + (\zeta_L^B - \zeta_L^A)^2}}{\sqrt{1 + \beta^2}}, \tag{41}$$

where β is given by (39), ζ_L^A and ζ_L^A can be expressed as functions of ζ_S^A and ζ_S^A using (25). We now have to determine the values of ζ_S^A and ζ_S^B that maximise $\Delta\overline{\omega}$ and are solution of eq. (40). The problem is solved graphically using the diagram reported in Fig. 12/(a). The contour plot herein shows the variation of $\Delta\overline{\omega}$ on the whole two-dimensional domain $0 \leq \{\zeta_S^A, \zeta_S^B\} \leq \pi$, while the red line reported in the same figure is the plot of eq. (40). Point Q, whose coordinates are solution of (40) and maximise $\Delta\overline{\omega}$, is denoted by the yellow dot. It corresponds to the intersection between the red line and the blue contour, the latter defined through eq. $\Delta\overline{\omega} = 1.46$. For the set of constitutive and geometrical parameters here considered, we have $\zeta_S^A = 1.215$ and $\zeta_S^B = 2.675$. By employing these values in eq. (25), we get $\zeta_L^A = 0.345$ and $\zeta_L^B = 0.769$, and then, eventually, $\beta = (\zeta_L^B - \zeta_L^A)/(\zeta_S^B - \zeta_S^A) = 0.284$. Therefore, this solution provides the slope of the flow segment corresponding to the widest lowest band gap, and its extremes $A(\zeta_S^A, \zeta_L^A)$ and $B(\zeta_S^A, \zeta_L^A)$ on the reduced torus $\mathbb{T}_3$ are marked with the red dots in Fig. 12/(b). This result is valid for any given value of $l_L \neq 0$ which is assumed to be known for the calculations, and then the optimisation procedure does not depend separately on lengths l_S and l_L, but only on their ratio β.

The illustrated method provides an exact solution to the problem of the maximisation of the lowest band gap, which is of practical importance in several operative scenarios involving different types of phononic structures (see, e.g. Sigmund and Sondergaard Jensen (2003); Liu et al. (2014); Hedayatrasa et al. (2016)). The formulation over the reduced torus can be easily extended to the case of an arbitrary cell $\mathcal{F}_i$ and represents a promising alternative to the direct approach based on partial evaluation of the frequency spectrum evaluation for all possible ratios l_S/l_L.

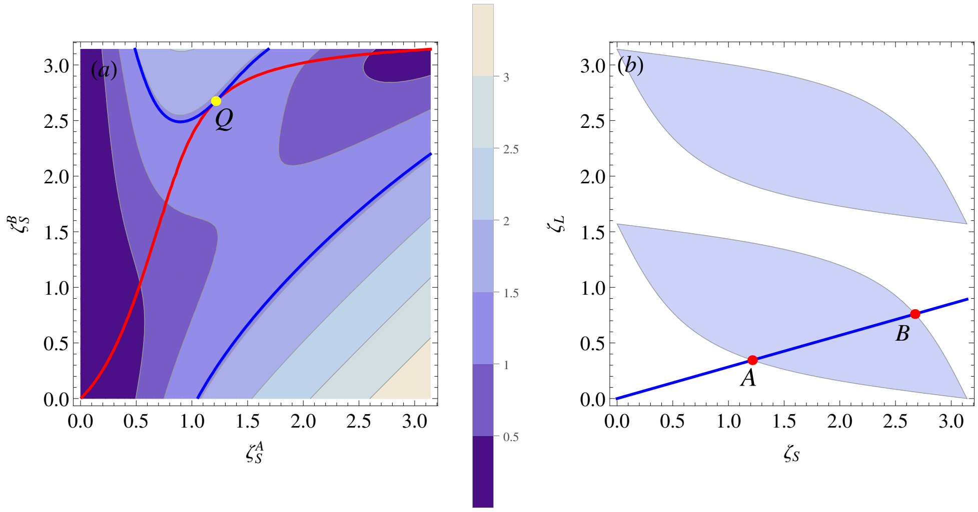

Figure 12: Optimisation of the lowest band gap for a waveguide designed according to parameters listed in Tab. 1. (a) Contour plot of the function $\Delta\overline{\omega}(\zeta_S^A, \zeta_S^B)$. Red and blue lines are associated with eqs. (40) and $\Delta\overline{\omega} = 1.46$, respectively. Point Q, marked in yellow, corresponds to $\zeta_S^A = 1.215$ and $\zeta_S^B = 2.675$, i.e. the solutions of eq. (40), and maximize $\Delta\overline{\omega}$. (b) Identification on $\mathbb{T}_3$ of the maximal lowest band gap obtained for $\beta = 0.284$ whose extremes are points A and B.

6 Scaling of the band gaps observed on the reduced torus

The universal representation of the spectrum on the reduced torus $\mathbb{T}_i$ can be exploited to check the local scaling occurring between band gaps at determined frequencies, as shown earlier in Gei (2010); Morini and Gei (2018); Morini et al. (2019) for different types of quasicrystalline phononic structures. Following their approach, let us identify with $R_i = (x_i, y_i, z_i)$ a point whose coordinates correspond to $x_i = \eta_{i+2}$, $y_i = \eta_{i+1}$ and $z_i = \eta_i$. On the basis of the recursive relation (11), the change of point R_i to R_{i+1} can be described as the evolution of the nonlinear discrete map

$$R_{i+1} = \mathcal{T}(R_i) = (x_{i+1}, y_{i+1}, z_{i+1}) = (2x_i y_i - z_i,\ x_i,\ y_i). \tag{42}$$

We can easily demonstrate (see, e.g. Gei (2010)) that the invariant

$$J(\omega) = J(\zeta_S(\omega), \zeta_L(\omega); \gamma) = x_i^2 + y_i^2 + z_i^2 - 2x_i y_i z_i - 1 = (\gamma^2 - 1)\sin^2\zeta_S(\omega)\sin^2\zeta_L(\omega) \tag{43}$$

is a constant, independent of index i. It is worth noting that $J = I/4$, where I is the Kohmoto's invariant defined in (Morini and Gei, 2018).

For any given value of the frequency, and then of the flux variables ζ_S and ζ_L, eq. (43) defines a manifold whose equation in the continuous three-dimensional space $Oxyz$ is $x^2 + y^2 + z^2 - 2xyz - 1 = J(\omega)$, the so-called Kohmoto's surface (Kohmoto and

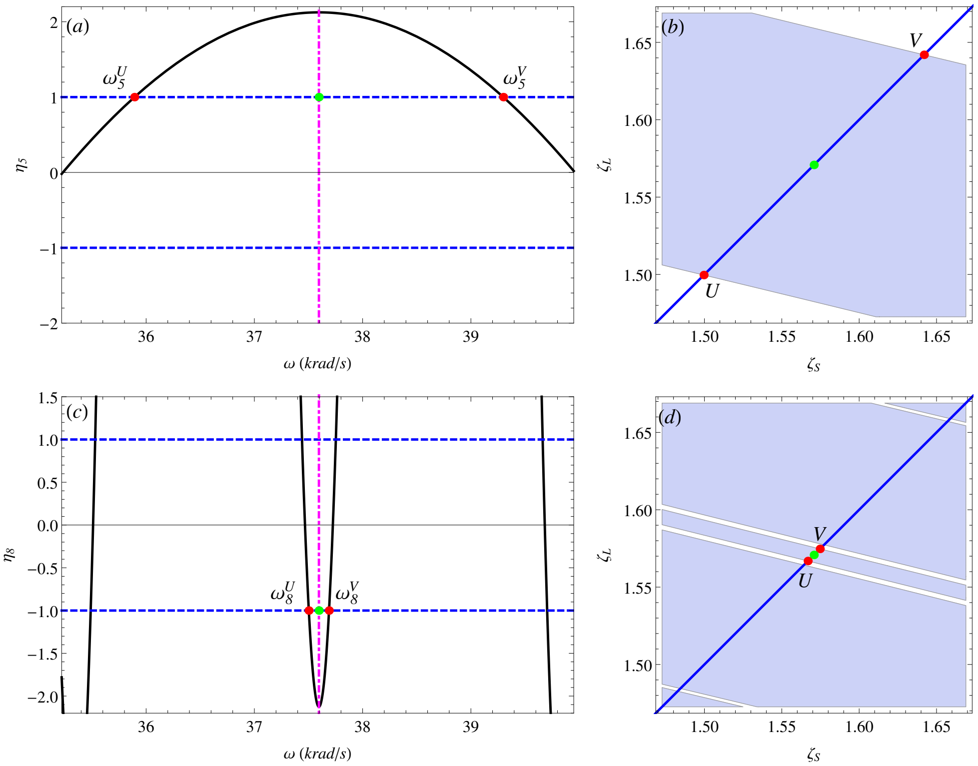

Figure 13: Half-trace diagrams (left) and flow lines on the domain $\mathbb{T}_i$ (right) corresponding to Fibonacci rods whose properties are listed in Tab. 1 with $l_S/l_L = 1$. Cells $\mathcal{F}_5$ ((a) and (b)) and $\mathcal{F}_8$ ((c) and (d)) are considered. The extremes of the band gap centered at the canonical frequency $\omega_c = 37.596$ krad/s, that is indicated with a green point, are marked with red points.

Oono, 1984). The points obtained by iterating map (42) are all confined on this surface and describe an open, *discrete* trajectory. Each Kohmoto's surface possesses six saddle points, say $\pm P_k$ $(k = 1, 2, 3)$, whose coordinates are $\pm P_1 = (\pm 2\sqrt{1 + J(\omega)}, 0, 0)$, $\pm P_2 = (0, \pm 2\sqrt{1 + J(\omega)}, 0)$, $\pm P_3 = (0, 0, \pm 2\sqrt{1 + J(\omega)}\,)$. They are connected through a closed (periodic) orbit generated by the six-cycle transformation obtained by applying six times map (42), in other words, $\mathcal{T}^6(P_k) = P_k$. Moreover, it can be also verified that $\mathcal{T}^3(P_k) = -P_k$. The frequencies ω_c at which a generic R_i coincides with one of these saddle points are called canonical frequencies and are exactly midway of the semi-period of the spectrum of canonical structures (Morini and Gei, 2018). For instance, in the cases addressed in Figs. 3, 4, 5 and 7, the period is approximately 305 krad/s and canonical frequencies are approximately 305/4 krad/s and (3/4)305 krad/s.

In the neighbourhood of ω_c, the corresponding point R_i locates in the vicinity of a saddle point, therefore the *discrete* trajectory traced by transformation of the point R_i itself at increasing index on the Kohmoto's surface is then studied as a small perturbation of the periodic orbit with map (42) linearised about the six saddle points. The derived linearised transformation has an eigenvalue that is equal to one and an additional pair of them given by

$$\kappa^{\pm}(\omega) = \left(\sqrt{1 + 4(1 + J(\omega))^2} \pm 2(1 + J(\omega)) \right)^2. \tag{44}$$

In both (Gei, 2010) and (Morini and Gei, 2018), it is shown that the quantity $\kappa^+(\omega)$ governs the local scaling occurring between localised ranges of the spectrum of cell $\mathcal{F}_i$ and that of $\mathcal{F}_{i+6}$, while $\lambda \approx \sqrt{\kappa^+}$ is the scaling factor between $\mathcal{F}_i$ and $\mathcal{F}_{i+3}$. In particular, across a canonical frequency, the width of a band gap in the diagram of cell $\mathcal{F}_{i+6}$ centred at frequency ω_c, say $\{\omega^V_{i+6} - \omega^U_{i+6}\}$, is related to that of $\{\omega^V_i - \omega^U_i\}$ in the diagram of cell $\mathcal{F}_i$ centred at the same frequency by the following scaling law

$$\omega^V_{i+6} - \omega^U_{i+6} \approx \frac{\omega^V_i - \omega^U_i}{\kappa}, \tag{45}$$

where $\kappa = \kappa^+(\omega_c)$. Similarly, the following relationship can be established between the widths of $\{\omega^V_{i+3} - \omega^U_{i+3}\}$ and $\{\omega^V_i - \omega^U_i\}$:

$$\omega^V_{i+3} - \omega^U_{i+3} \approx \frac{\omega^V_i - \omega^U_i}{\lambda}. \tag{46}$$

As a way of an example, let us consider Fibonacci canonical cells $\mathcal{F}_i$ whose parameters are those in Tab. 1 ($\gamma \approx 2.125$) and $l_S/l_L = 1$ ($\beta = 1$). For this class of structures, local scaling governed by (45) and (46) at $\omega_c = 37.596$ krad/s is analysed. The numerical results are illustrated in Fig. 13, where the band gap associated with $\mathcal{F}_5$ is compared with that corresponding to $\mathcal{F}_8$ using close up views of both the diagrams η_5 and η_8 (respectively (a) and (c)) and the flow lines on the reduced tori $\mathbb{T}_5$ and $\mathbb{T}_8$ (respectively (b) and (d)). The canonical frequency ω_c is indicated with green points and the magenta dot-dashed vertical lines on the left-hand sides, while the extremes of the band gaps U and V are denoted by the red points on the right. We note also in this case the perfect correspondence between the band gaps detected through the trace diagrams and the intersections of the flow lines with the subdomains $\mathbb{D}_5$ and $\mathbb{D}_8$. Concerning the band gap reported in Figs. 13/(a) and /(b), numerical calculations yield $\omega^V_5 - \omega^U_5 = 3.407$ krad/s and $\lambda = 18.12$. By using the relationship (46), the value $\omega^V_8 - \omega^U_8 \approx (\omega^V_5 - \omega^U_5)/\lambda = 0.188$ krad/s is obtained, which is in very good agreement with the value provided by direct estimation of the band gap highlighted in Figs. 13/(c) and /(d) (i.e. $\omega^V_8 - \omega^U_8 = 0.186$ krad/s). We record the same scaling behaviour by comparing $\omega^V_5 - \omega^U_5$ with $\omega^V_{11} - \omega^U_{11}$ centred at the same ω_c. In this case, the scaling factor is $\kappa = \kappa^+(\omega_c) = 328.25$, the actual range $\omega^V_{11} - \omega^U_{11}$ measures 0.0103 krad/s whereas relationship (45) provides $\omega^V_{11} - \omega^U_{11} \approx (\omega^V_5 - \omega^U_5)/\kappa = 0.0104$ krad/s.

The proposed example demonstrates how, in addition to the standard representation of the dispersion diagram, the typical scaling properties can be also pinpointed and estimated through the universal representation of the torus.

7 Concluding remarks

The characteristic features of the frequency spectrum for elastic waves propagating in a two-phase periodic medium can be revealed through its universal representation on a two-dimensional toroidal surface composed of pass band and band gap sub-regions. Frequency-dependent flow lines belonging to the surface can be defined for each configuration of the waveguide. In this paper, we exploited this possibility to investigate axial waves for a class of periodic rods whose elementary cell is generated through the Fibonacci substitution rule, an example of quasicrystalline sequence.

First, we have established the mechanical and geometrical conditions for which an elementary cell of the Fibonacci sequence may display closed flow lines on the torus, a circumstance that corresponds to the periodicity of the frequency spectrum and of the layout of pass bands and band gaps. We concluded that the required combination of parameters corresponds to that leading to the concept of *canonical* structures introduced by Morini and Gei Morini and Gei (2018). For these type of arrangements, it turned out that the band gap density depends on the lengths of the two phases. Conversely, for non-canonical rods, the flow lines cover ergodically the torus and their band gap density is independent of the lengths of the constituents.

Second, we addressed analytically two illustrative band gap optimisation problems, based on element $\mathcal{F}_3$ of the Fibonacci sequence. Analytical expressions of the boundaries of band gap regions on the torus were exploited, on the one hand, to guide the design of the elementary cell to achieve the widest low-frequency band gap, on the other, to detect the maximal band gap in the spectrum for a given configuration. Thanks to the availability of the expressions of the boundaries of the band-gap regions on the torus, the proposed optimisation technique is considerably more robust in comparison with the standard procedure based on partial evaluation of the frequency spectrum Sigmund and Sondergaard Jensen (2003); Liu et al. (2014); Hedayatrasa et al. (2016) which necessarily relies on numerical algorithms.

In the final section, the local scaling governing the spectrum of quasicrystalline-generated phononic rods about certain relevant frequencies, as revealed in Morini and Gei (2018), was investigated and confirmed through the analysis of the flow lines on the torus.

The presented approach based on the representation of pass band and band gap sub-regions on the toroidal manifold can be easily extended to study other wave phenomena governed by an equation similar to (2) in different periodic systems, i.e. prestressed laminates, photonic crystals and composite nanostructures. Moreover, through the definition of an appropriate set of invariants that fully characterize the pass band/band gap layout, similar universality properties can be detected in spectra associated with different types of equations, such as for example those related to flexural systems (Romeo and Luongo, 2002; Carta and Brun, 2015), thin soft dielectric films (Shmuel and Pernas-Salomon, 2016) and plane strain laminates (Chen et al., 2008).

Acknowledgements. This project has received funding from the European Union's Horizon 2020 research and innovation programme under Marie Skodowska-Curie Actions COFUND grant SIRCIW, agreement No 663830.

References

Arnold, V., 1989. Mathematical Methods of Classical Mechanics. Springer-Verlag, New York.

Band, R., Berkolaiko, G., 2013. Universality of the momentum band density of periodic networks. Phys. Rev. Lett. 111, 130404.

Barra, F., Gaspard, P., 2000. On the level spacing distribution in quantum graphs. J. Stat. Phys. 101, 283–319.

Berkolaiko, G., Winn, B., 2010. Relationship between scattering matrix and spectrum of quantum graphs. Trans. Am. Mat. Soc. 362, 6261–6277.

Brun, M., Guenneau, S., Movchan, A., Bigoni, D., 2010. Dynamics of structural interfaces: filtering and focussing effects for elastic waves. J. Mech. Phys. Solids 58, 1212–1224.

Brun, M., Slepyan, L., Movchan, A., 2013. Transition wave in a supported heavy beam. J. Mech. Phys. Solids 61, 2067–2085.

Carta, G., Brun, M., 2015. Bloch-Floquet waves in flexural systems with continous and descrete elements. Mech. Mat. 87, 11–26.

Chen, A.-L., Wang, Y.-S., Guo, Y.-F., Wang, Z.-D., 2008. Band structures and Fibonacci phononic quasicrystals. Solid State Comm. 145, 103–108.

Cherkaev, A., Cherkaev, E., Slepyan, L., 2005. Transition waves in bistable structures. I. Delocalization of damage. J. Mech. Phys. Solids 53, 383–405.

Colquitt, D., Brun, M., Gei, M., Movchan, A., Movchan, N., Jones, I., 2014. Transformation elastodynamics and cloaking for flexural waves. J. Mech. Phys. Solids 72, 131–143.

Ewing, M., Jardetzky, W., Press, F., 1956. Elastic waves in layered media. McGraw-Hill.

Gei, M., 2010. Wave propagation in quasiperiodic structures, stop/pass band distribution and prestress effects. Int. J. Solids Struct. 47, 3067–3075.

Guenneau, S., Movchan, A. B., Petursson, G., Ramakrishna, S. A., 2007. Acoustic metamaterials for sound focusing and confinement. New J. Phys. 9, 399.

Hedayatrasa, S., Abhary, K., Uddin, M.-S., Guest, J., 2016. Optimal design of tunable phononic bandgap plates under equibiaxial stretch. Smart Mat. Struct. 25, 055025.

Katok, A., Hasselblatt, B., 1996. Introduction to the modern theory of dynamical systems. Cambridge University Press.

Kohmoto, M., Oono, Y., 1984. Cantor spectrum for an almost periodic Schroedinger equation and a dynamical map. Phys. Lett. 102A, 145–148.

Kohmoto, M., Sutherland, B., Tang, C., 1987. Critical wave functions and a Cantor-set spectrum of a one-dimensional quasicrystal model. Phys. Rev. B 35, 1020–1033.

Kolar, M., 1993. New class of one dimensional quasicrystals. Phys. Rev. B 47, 5498–5492.

Kolar, M., Ali, M., 1989. Generalized Fibonacci superlattices, dynamical trace maps, and magnetic excitations. Phys. Rev. B 39, 426–432.

Krylov, V., Parnes, R., Slepyan, L., 1998. Nonlinear waves in an inextensible flexible helix. Wave Motion 27, 117–136.

Lekner, J., 1994. Light in periodically stratified media. J. Opt. Soc. Am. A 11, 2892–2899.

Liu, Z.-F., Wu, B., He, C.-F., 2014. Band-gap optimization in two-dimensional phononic crystals based on genetic algorithm and FPWE. Waves Rand. Compl. Media 24, 286–305.

Lustig, B., Shmuel, G., 2018. On the band gap universality of multiphase laminates and its applications. J. Mech. Phys. Solids 117, 37–53.

Mead, D., 1998a. Passive Vibration Control. Wiley, Chichester, U.K.

Mead, D., 1998b. Wave propagation in continous periodic structures: research contributions from Southampton, 1964-1995. J. Sound Vibr. 190, 495–524.

Mishuris, G., Movchan, A.B. Slepyan, L., 2009. Localised knife waves in a structured interface. J. Mech. Phys. Solids 57, 1958–1979.

Morini, L., Eyzat, Y., Gei, M., 2019. Negative refraction in quasicrystalline multilayered metamaterials. J. Mech. Phys. Solids 124, 282–298.

Morini, L., Gei, M., 2018. Waves in one-dimensional quasicrystalline structures: dynamical trace mapping, scaling and self-similarity of the spectrum. J. Mech. Phys. Solids 119, 83–103.

Nemat-Nasser, S., 1972. Harmonic wave propagation in layered composites. J. Appl. Mech. 39, 850–852.

Nieves, M., Mishuris, G., Slepyan, L., 2017. Transient waves in a transformable periodic flexural structure. J. Mech. Phys. Solids 112, 185–208.

Norris, A., 2008. Acoustic cloaking theory. Proc. Roy. Soc. A 464 (2097), 2411–2434.

Ott, E., 1993. Chaos in dynamical systems. Cambridge University Press.

Poddubny, A., Ivchenko, E., 2010. Photonic quasicrystalline and aperiodic structures. Physica E 43, 1871–1895.

Romeo, F., Luongo, A., 2002. Invariant representation of propagation properties for bi-coupled periodic structures. J. Sound Vib. 257, 869–886.

Rytov, S., 1956. Acoustical properties of a thinly laminated medium. Sov. Phys. Acoust. 2, 68–80.

Shmuel, G., Band, R., 2016. Universality of the frequency spectrum of laminates. J. Mech. Phys. Solids 92, 127–136.

Shmuel, G., Pernas-Salomon, R., 2016. Manipulating motions of elastomer films by electrostatically-controlled aperiodicity. Smart Mater. Struct. 25, 125012.

Sigmund, O., Sondergaard Jensen, J., 2003. Systematic design of phononic band-gap materials and structures by topology optimization. Phil. Trans. R. Soc. A 361, 1001–1019.

Slepyan, L., 2001a. Feeding and dissipative waves in fracture and phase transition. I. Some 1D structures and a square-cell lattice. J. Mech. Phys. Solids 49, 469–511.

Slepyan, L., 2001b. Feeding and dissipative waves in fracture and phase transition. II. Phase-transtion waves. J. Mech. Phys. Solids 49, 513–550.

Slepyan, L., 2001c. Feeding and dissipative waves in fracture and phase transition. III. Triangular-cell lattice. J. Mech. Phys. Solids 49, 2839–2875.

Slepyan, L., 2010. Dynamic crack growth under Rayleigh wave. J. Mech. Phys. Solids 58, 636–655.

Slepyan, L., Cherkaev, A., Cherkaev, E., 2005. Transition waves in bistable structures. II. Analytical solution: Wave speed and energy dissipation. J. Mech. Phys. Solids 53, 407–436.

Slepyan, L., Krylov, V., Rosenau, P., 1998. Solitary waves in flexible, arbitrary elastic helix. J. Eng. Mech. 124, 966–970.

Srivastava, A., 2016. Metamaterial properties of periodic laminates. J. Mech. Phys. Solids 96, 252–263.

Steurer, W., 2004. Twenty years of structure research on quasicrystals. Part I. Pentagonal, octagonal, decagonal and dodecagonal quasicrystals. Acta Crystals 219, 391–446.

Steurer, W., Deloudi, S., 2008. Fascinating quasicrystals. Acta Crystals A64, 1–11.

Sutherland, B., Kohmoto, M., 1987. Resistance of a one-dimensional quasicrystal: Power-law growth. Phys. Rev. B 36, 5877–5886.

Willis, J. R., 2016. Negative refraction in a laminate. J. Mech. Phys. Solids 97, 10–18.